Supporting Information

Facile fabrication of exfoliated g-C$_3$N$_4$/MWCNTs/Fe$_3$O$_4$ ternary composites with multi-component functional synergy for high-performance microwave absorption

Huan Liu[†, a, b], Shengjin Wu [a, b], Qihong Wang [a, b], Zongrui Zheng [a, b], Hao Zhao [a, b], Yulai Zhao [a, b, c], Longqiang Xiao [a, b, c], Jingyu Cai [a, b, c], Zhen Lu [a, b, c], Xiangyu Yin [*, a, b, c], Linxi Hou [*, a, b, c]

[a]   College of Chemical Engineering, Fuzhou University, Fuzhou 350116, China

[b]   Qingyuan Innovation Laboratory, Quanzhou 362801, China

[c]   Fujian Key Laboratory of Advanced Manufacturing Technology of Specialty Chemicals, Fuzhou University, Fuzhou 350116, P. R. China

[*]Corresponding authors,

Prof. Xiangyu Yin (xyin65@fzu.edu.cn); Prof. Linxi Hou (lxhou@fzu.edu.cn)

A listing of the contents

(1) Experimental section

(2) Fig. S1. SEM images of (a,b) BCN, (c,d) CCN.

(3) Fig. S2. The low magnification TEM images, the HRTEM of (a-h) CN/C-Fe$_3$O$_4$-3, (i) the SAED pattern of CN/C-Fe$_3$O$_4$-3.

(4) Fig. S3. The XRD patterns of (a) C-Fe$_3$O$_4$ and CN/C-Fe$_3$O$_4$ composites, (b) FWHM value of (002) peak of BCN and CCN, (c) Schematic illustration of carboxylated process.

(5) Fig. S4. Full scan survey XPS spectra of (a)CCN and BCN, high-resolution XPS spectra of (b) C 1s, (c) N 1s, (d) O 1s of CCN and BCN, (e) the diagram of different N sites in the tri-s-triazine layer, (f) the content of different N and the peak area ratios of sp^2 N to sp^3 N in BCN and CCN.

(6) Fig. S5. Full scan survey XPS spectra of (a) C-Fe$_3$O$_4$ and CN/C-Fe$_3$O$_4$-3, high-resolution XPS spectra of (b) C 1s, (c) N 1s, (d) O 1s, (e) Fe 2p of CN/C-Fe$_3$O$_4$-3.

(7) Table. S1. The Surface areas of all samples.

(8) Fig. S6. N$_2$ adsorption−desorption isotherms of (a) C-Fe$_3$O$_4$, (c) CN/C-Fe$_3$O$_4$-1, (e) CN/C-Fe$_3$O$_4$-2, (g) CN/C-Fe$_3$O$_4$-3, and pore size distributions (using BJH model) of (b) C-Fe$_3$O$_4$, (d) CN/C-Fe$_3$O$_4$-1, (f) CN/C-Fe$_3$O$_4$-2, (h) CN/C-Fe$_3$O$_4$-3.

(9) Fig. S7. the minimum microwave RL curves with different thicknesses in the frequency range of 2−18 GHz of (a) BCN, (b) CCN.

(10) Fig. S8. Real part of permittivity (ε') and imaginary part of permittivity (ε'') in the frequency range of 2−18 GHz of (a) BCN, (b) CCN.

(11) Table S2. MA performance of related absorbents in previous references.

(12) Fig. S9. (a) Schematic diagram of RCS simulation, 3D RCS values of (b) PEC, (c) C-Fe$_3$O$_4$, (d) CN/C-Fe$_3$O$_4$-1, (e) CN/C-Fe$_3$O$_4$-2, (f) CN/C-Fe$_3$O$_4$-3, RCS values (−60°~60°) of (g) PEC, C-Fe$_3$O$_4$, and CN/C-Fe$_3$O$_4$ composites.

Experimental section

Materials

Melamine ($C_3N_6H_6$), ferric chloride ($FeCl_3·6H_2O$), ferrous chloride ($FeCl_2·4H_2O$), ammonium hydroxide (NH_4OH, 25 wt.%) were purchased from Sinopharm Chemical Reagent Co., Ltd. Carboxylic multi-walled carbon nanotubes (purity: 95 %, outer diameter: 10−20 nm, inner diameter: 5−10 nm, length 10−30 μm, –COOH content: ~2 wt.%, special surface area: >200 m^2/g) were bought from Macklin. All chemical reagents were of analytical reagent grade and were used without further purification. Deionized water was obtained from an in-house water purification system.

Preparation of graphitic bulk carbon nitride (BCN)

In this way, graphitic carbon nitride (g-C_3N_4) is synthesized from melamine through thermal polycondensation. Typically, 10 g of melamine was put into a semi-closed ceramic crucible and calcined at 520 °C for 4 h in a muffle furnace with an increased rate of 10 °C min^{-1}. A light-yellow solid product obtained after the natural cooling of the crucible was bulk g-C_3N_4. Finally, the bulk g-C_3N_4 was ground into powder for further use.

Preparation of carboxylated g-C_3N_4(CCN)

Carboxylated g-C_3N_4 was prepared following the method of the previously reported literature. Briefly, 1.0 g of as-prepared BCN was put into 100 mL 5.0 M HNO_3 and refluxed at 125 °C for 24h. After naturally cooling to room temperature, the refluxed products were centrifuged and washed with deionized water several times until the pH

reached 7.0. The final products were freeze-dried for 24 h, and the obtained carboxylated g-C_3N_4 were labeled as CCN.

Preparation of g-C_3N_4/MWCNTs-Fe_3O_4 nanocomposites (CN/C-Fe_3O_4)

To begin, the carboxylated g-C_3N_4 dispersion was prepared according to the procedure for preparing CCN. The centrifuged precipitate and 0.1g of carboxylated MWCNTs were ultrasonically dispersed in 50 mL deionized water for 1h, then stirred for 2h. A typical in situ co-precipitation method was used to decorate Fe_3O_4 nanoparticles on CCN and MWCNTs. In the presence of inert gas, 2.62 g $FeCl_3 \cdot 6H_2O$ and 1.11 g $FeCl_2 \cdot 4H_2O$ were added to the suspension and stirred for 3h to ensure sufficient adsorption of iron ions onto the surface of MWCNTs and CCN. In the next step, aqueous ammonia (NH_4OH, 25%) was added dropwise to adjust the pH level to 10, and then the temperature was increased to 70 °C to facilitate the reaction for 2 hours with mechanical stirring. It was then collected using an external magnetic field and repeatedly washed with deionized water and ethanol. Finally, the products were dried at 60 °C under a vacuum. The samples with different weights of g-C_3N_4 (0 g, 0.5 g, 1.0 g, 1.5 g) were labeled as C-Fe_3O_4, CN/C-Fe_3O_4-1, CN/C-Fe_3O_4-2, CN/C- Fe_3O_4-3.

Characterization

Scanning electron microscopy (TESCAN MIRA LMS, Czech Republic), energy dispersive spectroscopy (EDS), and transmission electron microscopy (TEM; FEI TALOS F200X, operating voltage 200 kV) were used to analyze the morphology, element distribution, and microstructure of CN/C-Fe_3O_4. The phase composition and crystal structure were determined by X'pert3 powder X-ray diffractometer with Cu-Kα

radiation ($\lambda = 0.15406$ nm, 40 kV, 40 mA). Fourier transform infrared spectroscopy (FTIR) spectra of CN/C-Fe$_3$O$_4$ were performed by an FTIR infrared spectrometer (Thermo Scientific, iS50) in the range of 400 to 4000 cm^{-1}. Element composition and valence band information was analyzed by X-ray photoelectron spectroscopy (XPS, K-alpha, Thermo Fisher Scientific) and calibrated by C 1s peak of 284.6 eV. Nitrogen sorption isotherms were obtained at -196 °C by means of V−Sorb 2800TP. A Varian Cary 500 spectrophotometer was used to measure UV−Vis diffuse reflectance spectra (UV−Vis DRS). Electrical conductivity was measured on an electric powder conductivity tester (ST2742B) with four-probe method under 20 MPa.

A vector network analyzer Agilent N5234A was used to measure the electromagnetic parameters of absorbers over a frequency range of 2–18 GHz with the coaxial-line method. The coaxial test samples for electromagnetic measurements were prepared by mixing physically with paraffin (50 wt.% paraffin /50 wt.% absorber) and pressing them into cylindrical rings with an outer diameter of 7.00 mm, an inner diameter of 3.00 mm, and a thickness of 2.5–3.5 mm.

RCS simulation

The RF module of COMSOL Multiphysics 6.0 software was used to simulate the far-field RCS of a microwave absorber. A two-layer square plane (0.2 m × 0.2 m) was modeled, with an upper and lower layer of 2 mm thick absorbing and perfect electric conductor (PEC) layers, respectively. The background scattering field waveform is defined as a linearly polarized plane wave to simulate the emitted microwave of a radar at infinity, and the microwave propagate negatively along the Z-axis. Additionally, the

direction of scattering is determined by θ and φ. The radar cross section (RCS) of the simulated sample is given by the following equation:

$$\sigma\left(\mathrm{dBm}^2\right)=10\log\left[\frac{4\pi\mathrm{S}}{\lambda^2}\left|\frac{\mathrm{E_s}}{\mathrm{E_i}}\right|^2\right]$$

(1)

Where S represents the area of the simulated plate, λ is the wavelength of the microwave, E_s and E_i correspond to the electric field intensity of the scattered wave and the incident wave, respectively.
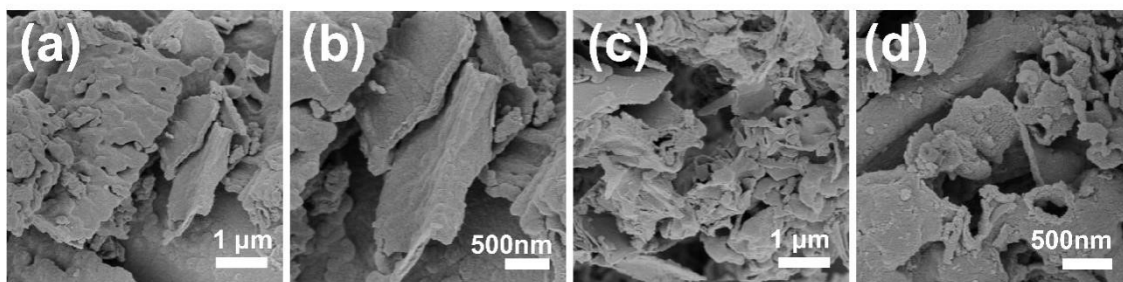
Fig. S1. SEM images of (a,b) BCN, (c,d) CCN.

Fig. S1(a,b) shows the morphology of the synthesized bulk g-C_3N_4. The BCN consists of thick, irregularly stacked sheets of several microns in size. After nitric acid treatment, the BCN were sheared into smaller fragments (**Fig. S1(c,d)**), which were thinner and more irregular, and stacked together to form a porous structure.
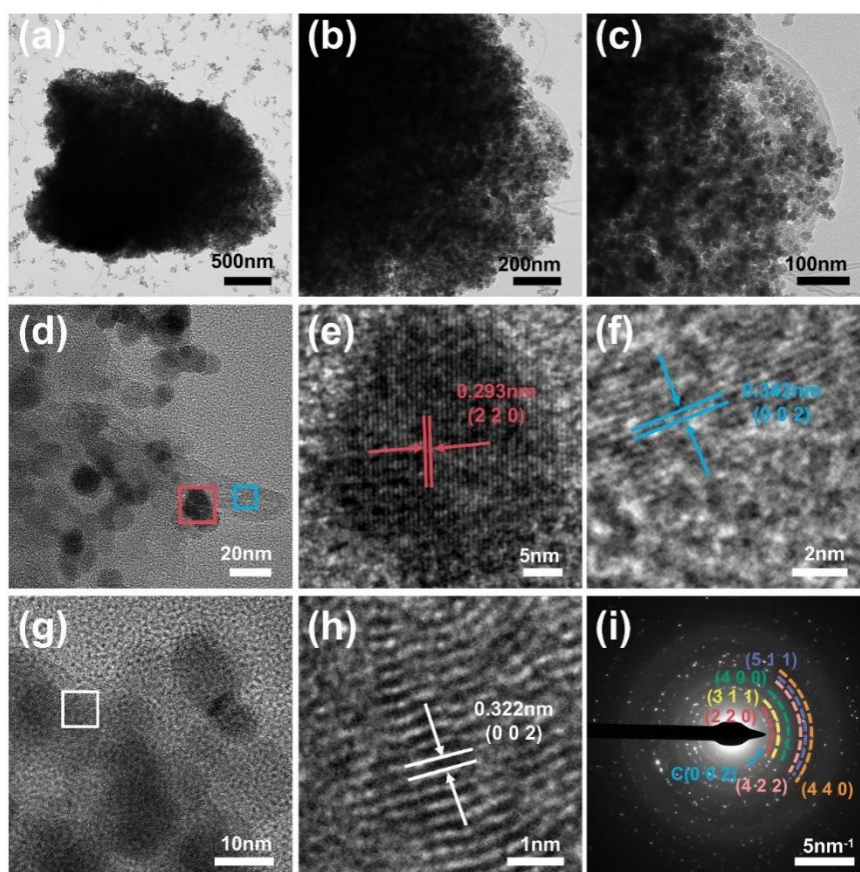
Fig. S2. The low magnification TEM images, the HRTEM of (a-h) CN/C-Fe3O4-3, (i) the SAED pattern of CN/C-Fe_3O_4-3.

Fig. **S2(a-c)** show that dense Fe_3O_4 nanoparticles were encapsulated around the nanosheets, and the filamentary structure at the edges corresponds to carbon nanotubes, which is consistent with the SEM images. The lattice structure can be directly observed based on the HRTEM images. The lattice spacing of 0.293 nm in **Fig. S2(e)** corresponds to the (220) crystal plane of Fe_3O_4[1], and the lattice spacing of 0.342 nm and 0.322 nm in **Fig. S2(f)** and **Fig. S2(h)** correspond to the (002) crystal plane of MWCNTs and CCN[2,3], respectively. The lattice defects may be caused by the loading of Fe_3O_4. The SAED pattern in **Fig. S2(i)** shows the diffraction rings of Fe_3O_4 and graphitized carbon, further verifying the crystal structure of CN/C-Fe_3O_4.
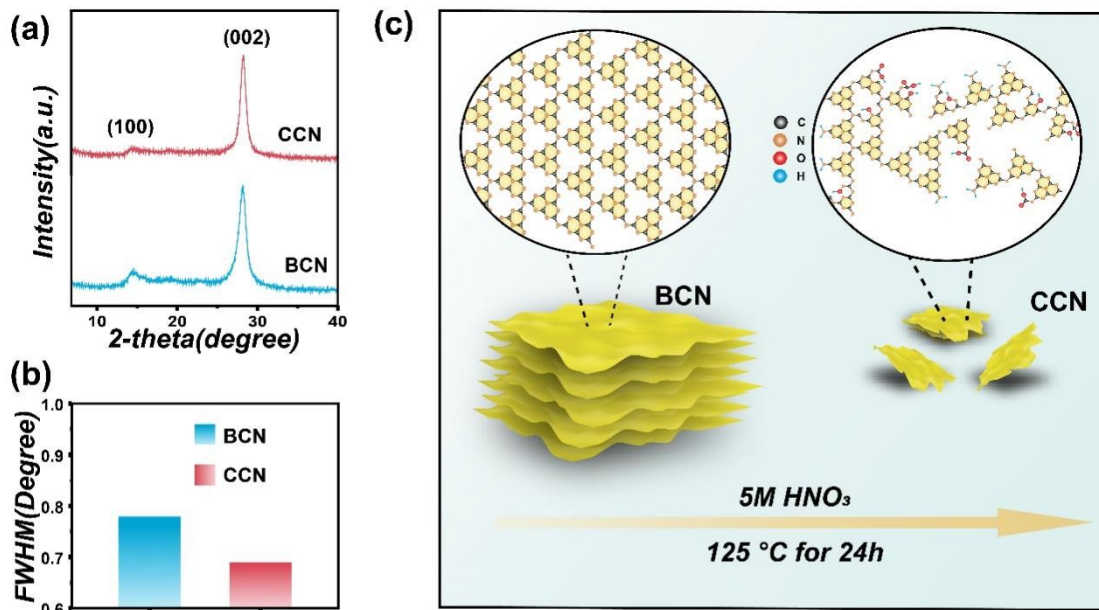
Fig. S3. The XRD patterns of (a) C-Fe$_3$O$_4$ and CN/C-Fe$_3$O$_4$ composites, (b) FWHM value of (002) peak of BCN and

CCN, (c) Schematic illustration of carboxylated process.

BCN reveals two typical peaks, the strong peak at 27.48° (d=0.324 nm) corresponds

to a characteristic inter-planar stacking reflection of the conjugated aromatic structure,

indexed for graphitic materials as the (002) peaks[4, 5]. Another peak at 13.10° (d=0.675

nm) is assigned to in-plane tri-s-triazine structure units, indexed as the (100) crystal

plane of g-C$_3$N$_4$[6]. After the carboxyl process of bulk g-C$_3$N$_4$, the characteristic (002)

inter-planar stacking peaks are still observed in the XRD pattern of CCN, indicating that

the carboxyl process does not destroy the graphite-like structure of g-C$_3$N$_4$[7]. Moreover,

the peak at 27.48° shifts to 27.64° (d=0.322 nm)[3]. This indicates a decreased interlayer

stacking distance between the basic sheets in the g-C$_3$N$_4$ nanosheets[8, 9], which can be

ascribed to π-π stacking and hydrogen bonding interactions[5, 10]. The oxidized layers can

be more planarized with a carboxylation treatment, leading to a denser packing, thus

reducing the gallery distance observed, which demonstrates that the layered g-C_3N_4 has been gradually exfoliated[7]. Moreover, the **Fig. S3(b)** shows the (002) plane full width at half maximum (FWHM) of the XRD pattern. The FWHM value for carboxylated g-C_3N_4 decreases with a carboxylated process, indicating that non-stable structures of not-well-ordered g-C_3N_4 nanosheets were removed and thus crystallinity of CCN was slightly improved[11]. Besides, the low-angle peak of the (100) plane is weak in the XRD pattern of CCN, indicating the simultaneously reduced size of nanosheets during protonation depolymerization of the in-plane tri-s-triazine structural packing motif[12].
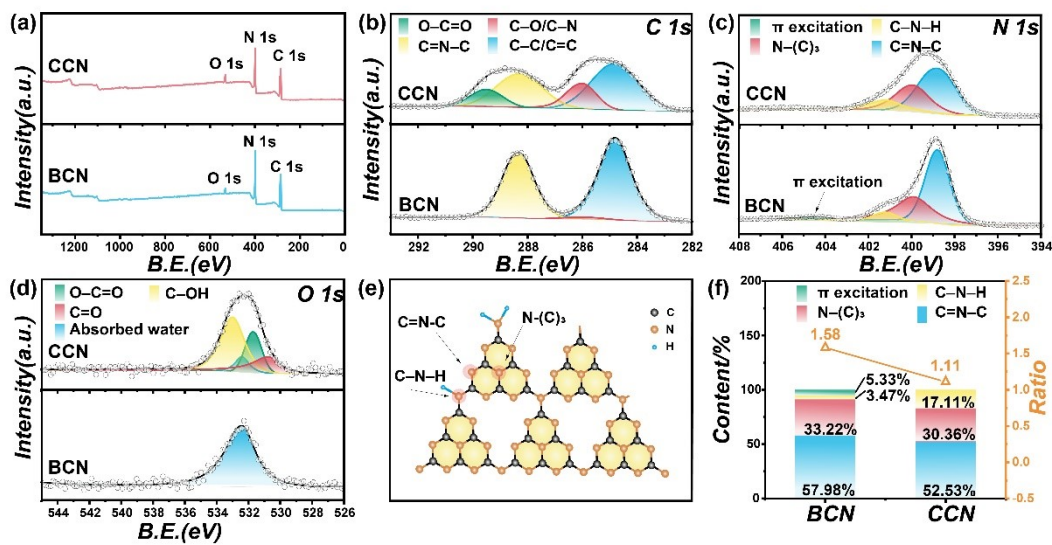
Fig. S4. Full scan survey XPS spectra of (a)CCN and BCN, high-resolution XPS spectra of (b) C 1s, (c) N 1s, (d) O 1s of CCN and BCN, (e) the diagram of different N sites in the tri-s-triazine layer, (f) the content of different N and the peak area ratios of sp^2 N to sp^3 N in BCN and CCN.
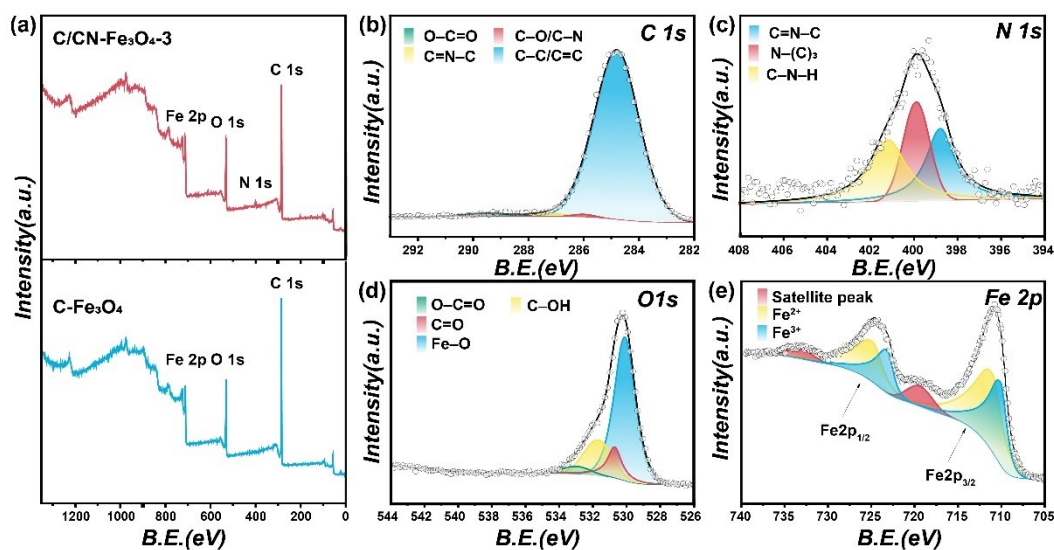
Fig. S5. Full scan survey XPS spectra of (a) C-Fe_3O_4 and CN/C-Fe_3O_4-3, high-resolution XPS spectra of (b) C 1s, (c) N 1s, (d) O 1s, (e) Fe 2p of CN/C-Fe_3O_4-3.

According to the full scan survey spectra (**Fig. S4(a)**, **Fig. S5(a)**), CCN and BCN are mainly composed of C, N, and O, while C-Fe_3O_4 is composed of C, O, Fe. For CN/C-Fe_3O_4, the appearance of N 1s peak can ascribe to the introduction of CCN.

The C 1s spectra of BCN (**Fig. S4(b)**) shows three characteristic peaks at 284.8 eV, 286.0 eV and 288.3 eV, corresponding to the graphitic carbon (C=C/C–C bonds), sp^2-bonded carbon (N=C–N coordination), and C–O/C–N bonds, respectively[13]. Compared with BCN, a new peak at 289.5 eV appears in CCN, corresponding to the –COOH species[14]. As shown in **Fig. S5(b),** C 1s spectra of CN/C-Fe_3O_4-3 exhibits the strongest graphitic carbon peak and the other weak peak, which can be ascribed to the presence of MNCNTs and the surface of CCN being covered by Fe_3O_4 particles.

The N 1s spectrum (**Fig. S4(c)**, **Fig. S5(c)**) can be deconvoluted into three peaks at 398.6 eV, 399.9 eV, and 401.0 eV, denoting sp^2-hybridized nitrogen (C=N–C bonds), sp^3-hybridized tertiary nitrogen (N–(C)$_3$), and amino groups (C–N–H), respectively[15].

S13

Fig. S4(e) exhibits the diagram of different N sites in the tri-s-triazine layer. As for CCN, the extra broad peaks at about 404.1 eV can be attributed to charging effects or π excitation[16]. The peak area ratios of sp^2 N to sp^3 N in BCN and CCN, are calculated to be 1.58 and 1.11 (**Fig. S4(f)**), indicating that the oxidation of the cutting process preferentially proceeded at C=N–C bonds of the tris-s-triazine. These results are consistent with the XRD and FTIR analyses.

Fig. S4(d) and **Fig. S5(d)** shows the O 1s of the samples, the peak at 532.4 eV in the BCN is assigned to the absorbed water[17]. Compared with BCN, the strong O 1s peak indicates the presence of oxygen-containing groups in CCN, which could be deconvoluted into four peaks. Three new peaks are located at 530.7 eV, 531.8 eV, and 533.1 eV, corresponding to the O=C–OH, C=O, and C–OH groups, respectively[18]. For $CN/C-Fe_3O_4$ as well as $C-Fe_3O_4$, the O 1s spectrum shows not only oxygen-containing groups but also Fe–O bonds at 530.1 eV, indicating the presence of Fe_3O_4[19]. Further analysis of Fe 2p was performed, as shown in **Fig. S5(e)**, the peaks of Fe^{2+} are located at 710.1 and 723.1 eV, the peaks of Fe^{3+} are located at 711.0 and 724.8 eV, and the satellite peaks from ferric oxide particles are located at 719.4 and 733.2 eV.

Table S1. The Surface areas of all samples.

sample	BCN	CCN	C-Fe$_3$O$_4$	CN/C-Fe$_3$O$_4$-1	CN/C-Fe$_3$O$_4$-2	CN/C-Fe$_3$O$_4$-3
S$_{BET}$ (m^{2}g^{-1})	7.694	48.323	144.873	148.589	176.752	184.816

Surface area calculated from nitrogen adsorption isotherms at 77.3 K using the BET equation.
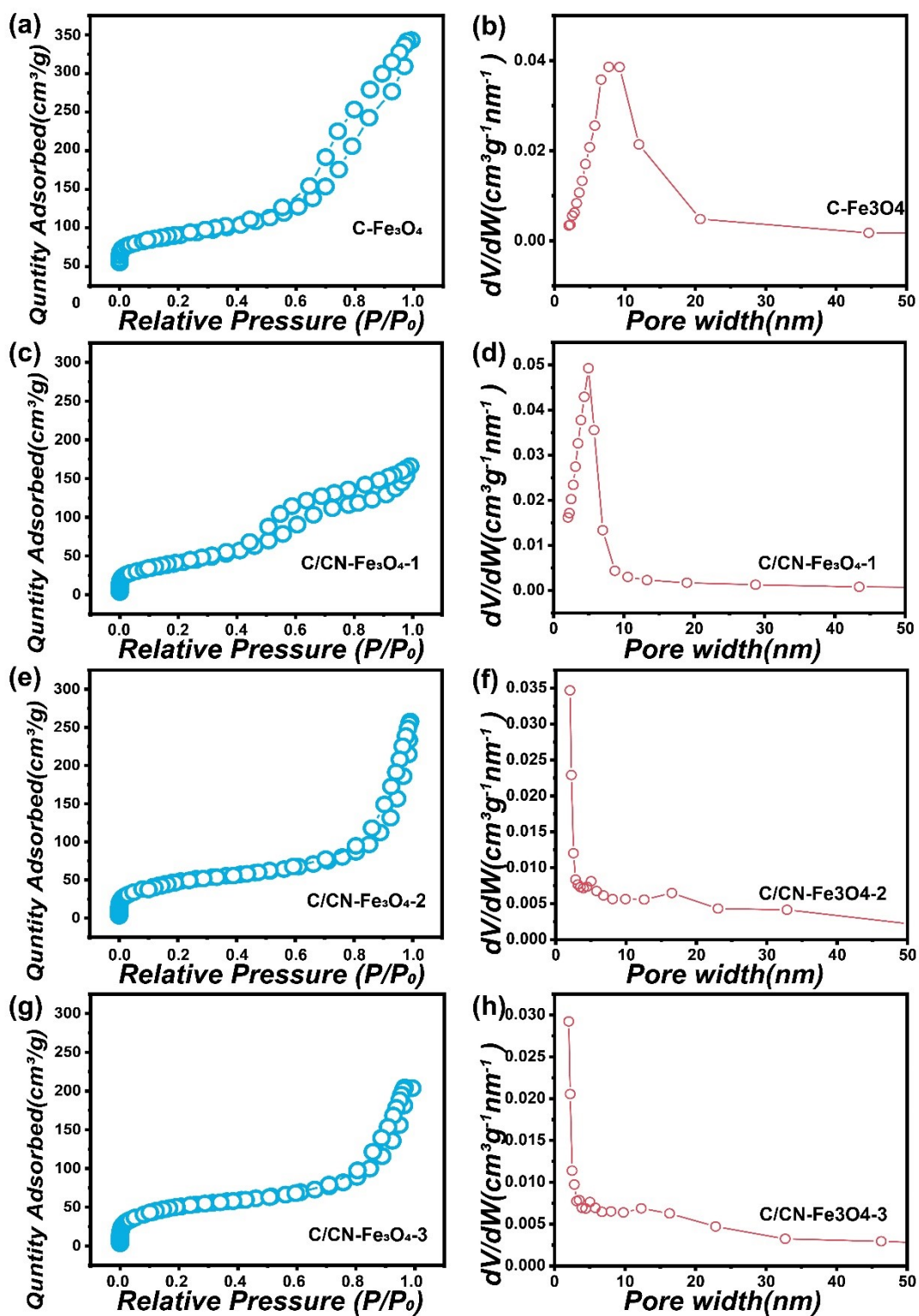
Fig. S6. N_2 adsorption−desorption isotherms of (a) $C-Fe_3O_4$, (c) $CN/C-Fe_3O_4-1$, (e) $CN/C-Fe_3O_4-2$, (g) $CN/C-Fe_3O_4-3$, and pore size distributions (using BJH model) of (b) $C-Fe_3O_4$, (d) $CN/C-Fe_3O_4-1$, (f) $CN/C-Fe_3O_4-2$, (h) $CN/C-Fe_3O_4-3$.
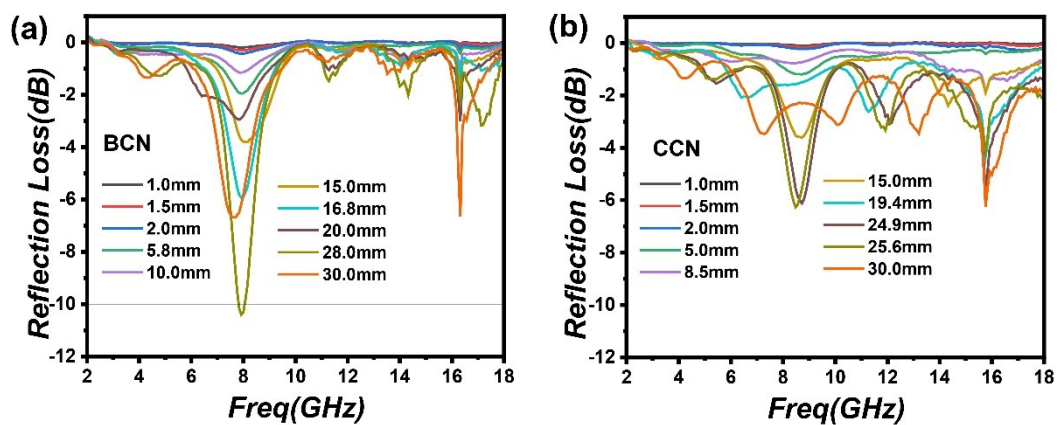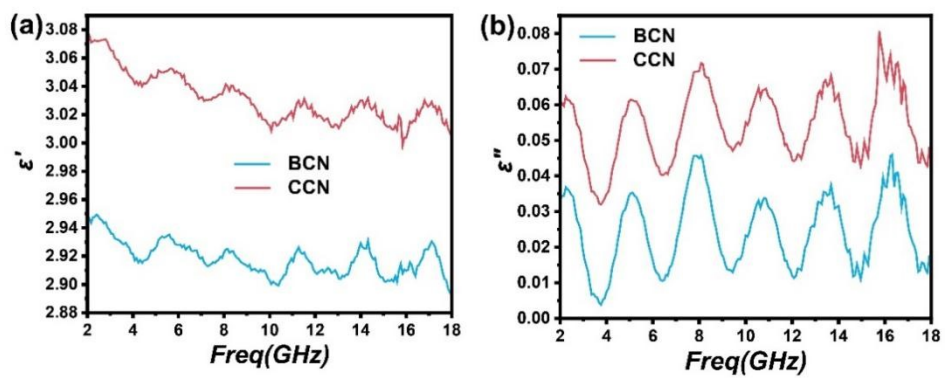
**Fig. S7.** the minimum microwave RL curves with different thicknesses in the frequency range of 2−18 GHz of (a) BCN, (b) CCN.

Fig. S8. Real part of permittivity (ε') and imaginary part of permittivity (ε'') in the frequency range of 2−18 GHz of (a) BCN, (b) CCN.

Table S2. MA performance of related absorbents in previous references.

Materials	Filler content (wt.%)	Matching thickness (mm)	RL_{min} (dB)	Effective bandwidth (GHz)	References
Co/ZnO/C	30	3	−52.6	4.9	[20]
ZnO/NPC@Co/NPC	50	1.9	−28.8	4.2	[21]
TiO2/Ti$_3$C$_2$Tx/Fe$_3$O$_4$	50	1.9	−57.3	2.0	[22]
CNT/Ni@N-C	30	2.5	−55.1	2.0	[23]
Co/C@CNTs-1	25	2.5	−55.8	4.1	[24]
CoNi-N/C-700	10	2.9	−50.7	4.6	[25]
CNTs/BaTiO$_3$/PANI	30	4.0	−30.9	2.7	[26]
Ni/NC/C-750	16	2.5	−45.2	4.5	[27]
FeNi@NGLs/NC	30	3.0	−47.8	4.8	[28]
LAS@rGO/CoFe$_2$O$_4$	30	2.3	−50	6.16	[29]
Fe/MnO@C	50	5.5	−45	5.0	[30]
MoS$_2$–Ni–CNTs	30	2.4	−50.08	6.04	[31]
FeSiAl@Al$_2$O$_3$@SiO$_2$	80	2.0	−46.29	7.33	[32]
Fe–Fe$_3$O$_4$@C	50	2.0	−46.29	3.6	[33]
CN/C-Fe$_3$O$_4$	50	1.9	−51.74	4.28	This work
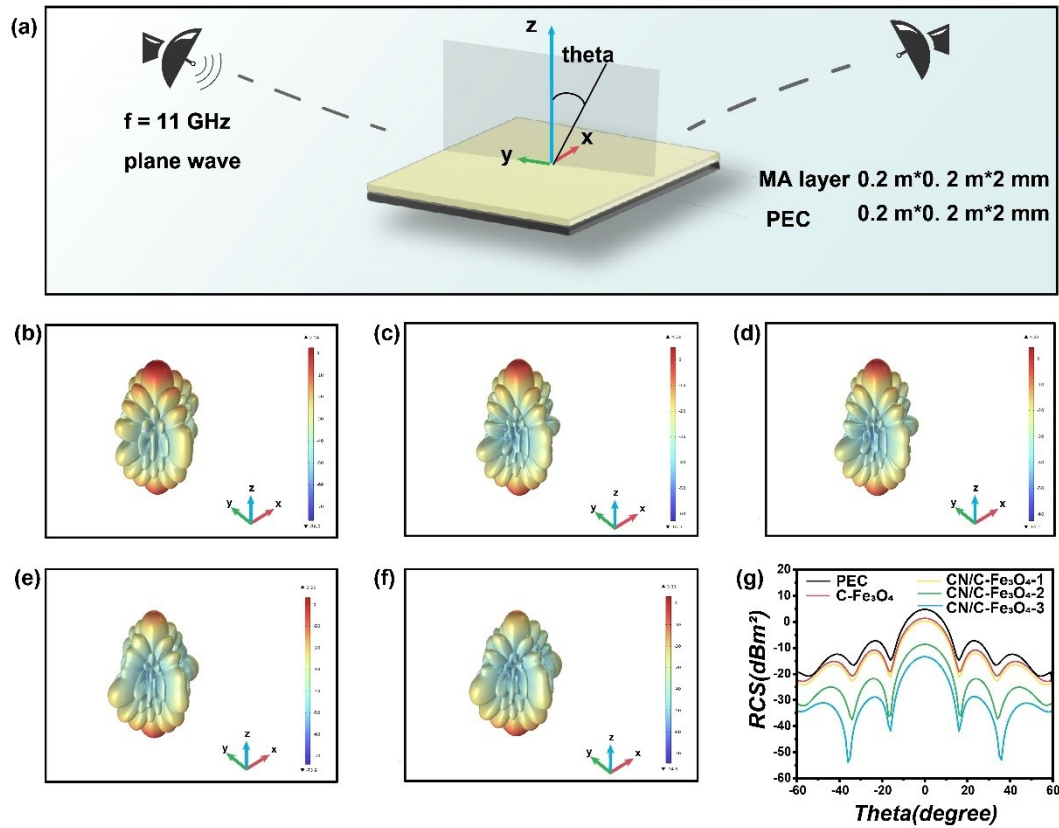
Fig. S9. (a) Schematic diagram of RCS simulation, 3D RCS values of (b) PEC, (c) C-Fe$_3$O$_4$, (d) CN/C-Fe$_3$O$_4$-1, (e) CN/C-Fe$_3$O$_4$-2, (f) CN/C-Fe$_3$O$_4$-3, RCS values (−60°~60°) of (g) PEC, C-Fe$_3$O$_4$, and CN/C-Fe$_3$O$_4$ composites.

To better simulate microwave absorption capability in practical applications, COMSOL software was used to calculate the simulated radar cross section (RCS) of a metal plate model coated with homogeneous absorbing material[34, 35]. As X-band radars are commonly used in defence applications, we selected 11 GHz as the simulation frequency. As shown in **Fig. S9(a)**, the established model involves a double-layer 2 mm square of 20*20 cm^2, which has a bottom coated with PEC and a top covered with C-Fe$_3$O$_4$ and CN/C-Fe$_3$O$_4$ composites. Plane waves incident along the Z axis and θ is the monitoring angle, with a range of changes of −60°~ 60°. Figure **Fig. S9(b-f)** compares

the 3D radar cross section (RCS) simulation results of the perfect conductor (PEC) and the composites, which accurately reflect real environments far-field absorption characteristics. As the microwave is incident vertically ($\theta=0°$), the scattering of the plate structure is the strongest (**Fig. S9(g)**). For $C\text{-}Fe_3O_4$, $CN/C\text{-}Fe_3O_4\text{-}1$, $CN/C\text{-}Fe_3O_4\text{-}2$, and $CN/C\text{-}Fe_3O_4\text{-}3$, the maximum reductions of RCS (the RCS of the PEC layer minus the RCS of the sample) are 3.38 dBm^2, 4.45 dBm^2, 13.40 dBm^2, and 18.12 dBm^2, respectively. This indicates that $CN/C\text{-}Fe_3O_4$ composites exhibit excellent radar wave attenuation, suppressing microwave reflection from the surface of PEC. $CN/C\text{-}Fe_3O_4\text{-}3$ shows the highest RCS reduction value, which indicates great potential in practical applications.

References

1. Y.-L. Ren, H.-Y. Wu, M.-M. Lu, Y.-J. Chen, C.-L. Zhu, P. Gao, M.-S. Cao, C.-Y. Li and Q.-Y. Ouyang, *ACS applied materials & interfaces*, 2012, **4**, 6436-6442.

2. O. V. Kharissova and B. I. Kharisov, *Rsc Advances*, 2014, **4**, 30807-30815.

3. A. Navarro-Aguilar, S. Obregón, D. Hernández-Uresti and J. Suárez-de La Cruz, *Research on Chemical Intermediates*, 2019, **45**, 3865-3878.

4. X. Li, X. Zhang, H. Ma, D. Wu, Y. Zhang, B. Du and Q. Wei, *Biosens Bioelectron*, 2014, **55**, 330-336.

5. M. Rong, L. Lin, X. Song, Y. Wang, Y. Zhong, J. Yan, Y. Feng, X. Zeng and X. Chen, *Biosens Bioelectron*, 2015, **68**, 210-217.

6. L. Ye, J. Liu, Z. Jiang, T. Peng and L. Zan, *Applied Catalysis B: Environmental*, 2013, **142**, 1-7.

7. S. Zhang, J. Li, M. Zeng, J. Xu, X. Wang and W. Hu, *Nanoscale*, 2014, **6**, 4157-4162.

8. G. Shiravand, A. Badiei and G. Mohammadi Ziarani, *Sensors and Actuators B: Chemical*, 2017, **242**, 244-252.

9. S. Yang, Y. Gong, J. Zhang, L. Zhan, L. Ma, Z. Fang, R. Vajtai, X. Wang and P. M. Ajayan, *Adv Mater*, 2013, **25**, 2452-2456.

10. H. J. Li, B. W. Sun, L. Sui, D. J. Qian and M. Chen, *Phys Chem Chem Phys*, 2015, **17**, 3309-3315.

11. H. Wei, Q. Zhang, Y. Zhang, Z. Yang, A. Zhu and D. D. Dionysiou, *Applied Catalysis A: General*, 2016, **521**, 9-18.

12. P. Li, Y. Wang, J. Wang, L. Dong, W. Zhang, Z. Lu, J. Liang, D. Pan and Q. Fan, *Chem. Eng. J.*, 2021, **414**.

13. C.-Q. Xu, K. Li and W.-D. Zhang, *Journal of colloid and interface science*, 2017, **495**, 27-36.

14. A. Kumar, S. Singh and M. Khanuja, *Materials Chemistry and Physics*, 2020, **243**, 122402.

15. H. Wei, Q. Zhang, Y. Zhang, Z. Yang, A. Zhu and D. D. Dionysiou, *Applied Catalysis A: General*, 2016, **521**, 9-18.

16. C. Ye, J.-X. Li, Z.-J. Li, X.-B. Li, X.-B. Fan, L.-P. Zhang, B. Chen, C.-H. Tung and L.-Z. Wu, *Acs Catalysis*, 2015, **5**, 6973-6979.

17. Y. Lei, D. Wang, J. Ji, J. Yan, X. Dong, J. Han, X. Liang, Q. Wei, X. Huang and X. Yu, *Journal of Environmental Chemical Engineering*, 2022, **10**, 107757.

18. H.-J. Li, B.-W. Sun, L. Sui, D.-J. Qian and M. Chen, *Physical Chemistry Chemical Physics*, 2015, **17**, 3309-3315.

19. J. Gu, H. Jia, S. Ma, Z. Ye, J. Pan, R. Dong, Y. Zong and J. Xue, *ACS omega*, 2020, **5**, 30980-30988.

20. Q. Liao, M. He, Y. Zhou, S. Nie, Y. Wang, S. Hu, H. Yang, H. Li and Y. Tong, *ACS applied materials & interfaces*, 2018, **10**, 29136-29144.

21. X. Liang, B. Quan, G. Ji, W. Liu, Y. Cheng, B. Zhang and Y. Du, *Inorganic Chemistry Frontiers*, 2016, **3**, 1516-1526.

22. P. Liu, V. M. H. Ng, Z. Yao, J. Zhou and L. B. Kong, *Materials Letters*, 2018, **229**, 286-289.

23. Y. Qiu, H. Yang, L. Ma, Y. Lin, H. Zong, B. Wen, X. Bai and M. Wang, *Journal of Colloid and Interface Science*, 2021, **581**, 783-793.

24. W. Liu, P. Duan, C. Mei, K. Wan, B. Zhang, H. Su, X. Zhang, J. Wang and Z. Zou, *Dalton Transactions*, 2021, **50**, 6222-6231.

25. L.-L. Liang, Z. Liu, L.-J. Xie, J.-P. Chen, H. Jia, Q.-Q. Kong, G.-H. Sun and C.-M. Chen, *Carbon*, 2021, **171**, 142-153.

26. L. Yu, C. Wang, F. Chen, J. Zhang, Y. Ruan and J. Xu, *Journal of Molecular Catalysis A: Chemical*, 2016, **411**, 1-8.

27. Y. Zhou, W. Zhou, C. Ni, S. Yan, L. Yu and X. Li, *Chem. Eng. J.*, 2022, **430**, 132621.

28. H. Yuan, Y. Wang, B. Suo, S. Zhang, H. Dong, F. Yan, C. Zhu and Y. Chen, *Journal of Alloys and Compounds*, 2021, **854**, 157212.

29. X. Zhang, L. Xia, B. Zhong, H. Yang, B. Shi, L. Huang, Y. Yang and X. Huang, *Journal of Alloys and Compounds*, 2019, **799**, 368-376.

30. G. He, Y. Duan and H. Pang, *Nano-Micro Lett.*, 2020, **12**, 1-16.

31. Y. Sun, J. Xu, W. Qiao, X. Xu, W. Zhang, K. Zhang, X. Zhang, X. Chen, W. Zhong and Y. Du, *ACS Applied Materials & Interfaces*, 2016, **8**, 31878-31886.

32. Y. Guo, X. Jian, L. Zhang, C. Mu, L. Yin, J. Xie, N. Mahmood, S. Dou, R. Che and L. Deng, *Chem. Eng. J.*, 2020, **384**, 123371.

33. X. Jian, X. Xiao, L. Deng, W. Tian, X. Wang, N. Mahmood and S. Dou, *ACS applied materials & interfaces*, 2018, **10**, 9369-9378.

34. D. Micheli, A. Vricella, R. Pastore and M. Marchetti, *Carbon*, 2014, **77**, 756-774.

35. D. Xuesong, D. Chenglong, W. Yahui, L. Zhigang, L. Cheng, C. Zongsheng, L. Xiangyin and S. Jiaming, *Plasma Science and Technology*, 2022, **24**, 114006.